npj | Computational Materials

www.nature.com/npjcompumats

ARTICLE OPEN

Thermodynamic potential and phase diagram for multiferroic bismuth ferrite ($BiFeO_3$)

Dmitry V. Karpinsky[1,2], Eugene A. Eliseev[3], Fei Xue[4], Maxim V. Silibin[2], Alexandra Franz[5], Maya D. Glinchuk[3], Igor O. Troyanchuk[2], Sergey A. Gavrilov[2], Venkatraman Gopalan[4], Long-Qing Chen[4] and Anna N. Morozovska[6]

We construct a Landau–Ginzburg thermodynamic potential, and the corresponding phase diagram for pristine and slightly doped bismuth ferrite, a ferroelectric antiferromagnet at room temperature. The potential is developed based on new X-ray and neutron diffraction experiments complementing available data. We demonstrate that a strong biquadratic antiferrodistortive-type coupling is the key to a quantitative description of $Bi_{1-x}La_xFeO_3$ multiferroic phase diagram including the temperature stability of the antiferromagnetic, ferroelectric, and antiferrodistortive phases, as well as for the prediction of novel intermediate structural phases. Furthermore, we show that "rotomagnetic" antiferrodistortive–antiferromagnetic coupling is very important to describe the ferroelectric polarization and antiferrodistortive tilt behavior in the *R3c* phase of $BiFeO_3$. The Landau–Ginzburg thermodynamic potential is able to describe the sequence of serial and trigger-type phase transitions, the temperature-dependent behavior of the order parameters, and the corresponding susceptibilities to external stimuli. It can also be employed to predict the corresponding ferroelectric and antiferrodistortive properties of $Bi_{1-x}La_xFeO_3$ thin films and nanoparticles by incorporating the gradient and surface energy terms that are strongly dependent on the shape, size, and preparation method.

npj Computational Materials (2017)3:20 ; doi:10.1038/s41524-017-0021-3

INTRODUCTION

State-of-the art

Multiferroics, defined as ferroics with more than one long-range order, are ideal systems for fundamental studies of couplings among the ferroelectric (FE) polarization, structural antiferrodistortion, and antiferromagnetic (AFM) order parameters.[1–5] $BiFeO_3$ (BFO) is the one of the rare multiferroics with a strong FE polarization, antiferromagnetism at room temperature as well as conduction and magnetotransport at domain walls.[6–8]

Multiferroic properties have also been extensively demonstrated $BiFeO_3$ thin films and heterostructures.[9–12] In particular, the studies of thin epitaxial $BiFeO_3$ films revealed a universal field induced phase transition, modulated phases and microstructure changes as a function of rare-earth (RE) elements (e.g., Dy, Sm, Ho) doping concentration.[13–17] Further RE doping effect was studied systematically for thin $BiFeO_3$ films, and it was shown experimentally and theoretically[16–18] that the doping of $BiFeO_3$ by Sm can lead to the enhancement of dielectric properties and tunability, as well as to the stabilization of the polar phase over a wide range of temperatures for the thin $(Bi,Sm)FeO_3$ films and the short period superlattices $BiFeO_3$–$(Bi,Sm)FeO_3$.

Bulk $BiFeO_3$ exhibits antiferrodistortive (AFD) order at temperatures below 1200 K; it is FE with a large spontaneous polarization below 1100 K and is AFM below Neel temperature $T_N \approx 650$ K.[19, 20] The very high AFD transition temperature of multiferroic $BiFeO_3$ offers the unique possibility to study the influence of AFD order on the FE and AFM phase transitions. Despite extensive experimental and theoretical studies of $BiFeO_3$ physical properties,[21–27] many important issues concerning the physical mechanisms responsible for the emergence and manifestation of its multiferroic and electrophysical properties remain unclear.[4–26] For example, the possibility of rare "trigger-type" phase transitions,[28] in which different order parameters appear simultaneously at the same transition temperature, is under debate in $BiFeO_3$.[29] Further, reliable experimental results and analysis[4–26] indicate the importance of the AFD-type couplings in $BiFeO_3$, such as biquadratic AFD–AFM and AFD–FE couplings, and different AFD order parameters regarded as "AFD–AFD" coupling. The antiferrodistortion comes from the static rotation of some atomic groups with respect to other parts of the crystal.[30] In this work, the term AFD-symmetry means only the static rotational symmetry of the oxygen octahedra MO_6 with respect to the cube A_8 cell in AFD perovskites with the structural formula AMO_3. Oxygen atoms are displaced with respect to the centers of the cube faces A_8 in the AFD phase, and the angle or the value of the corresponding displacement is a structural order parameter (see for e.g., ref. 31). According to group theory, the aforementioned biquadratic coupling can exist in all AFD multiferroics.[32]

Research motivation and impact

Our primary goal is to explain and describe quantitatively the experimental data obtained in pure $BiFeO_3$ and ab initio calculations performed previously, and in the process, construct a thermodynamic potential of Landau–Ginzburg (LG) type, which describes FE and AFD properties in pure $BiFeO_3$. Such a LG-potential is currently lacking that can be used to reconstruct the

[1]Scientific-Practical Materials Research Centre of NAS of Belarus, P. Brovki str., 19 Minsk 220072, Belarus; [2]National Research University of Electronic Technology "MIET", Bld. 1, Shokin sq. Zelenograd, Moscow 124498, Russia; [3]Institute for Problems of Materials Science, National Academy of Sciences of Ukraine, Krzhizhanovsky str., 3 Kyiv 03680, Ukraine; [4]Department of Materials Science and Engineering, Pennsylvania State University, University Park State College, PA 16802, USA; [5]Helmholtz Center Berlin, Hahn-Meitner-Platz 1, Berlin 14109, Germany and [6]Institute of Physics, National Academy of Sciences of Ukraine, 46, pr. Nauky Kyiv 03028, Ukraine
Correspondence: Dmitry V. Karpinsky (karpinski@ua.pt)

Received: 12 November 2016 Revised: 28 March 2017 Accepted: 10 April 2017
Published online: 15 May 2017

FE polarization and AFD tilts in the low temperature AFM phase as well as high temperature phases, which are known in addition to a new phase that is disclosed in this work. Further discussion testifies to the essential impact of the AFD order on the FE and AFM long-range order and provides theoretical background to the appearance of trigger-type phase transitions due to the strong biquadratic coupling.

Though the main subject of the investigations is pure bismuth ferrite, we have also included the case of slightly La-doping[4] (5%), which does not significantly change the structural parameters of the compound as compared to the pristine $BiFeO_3$ (which is necessary for theoretical fitting), but notably lowers the critical transition temperatures and thus increases the reliability of the structural measurements at elevated temperatures. Thus the slightly doped compound with virtually no difference in the multiferroic behavior and a phase diagram as compared with pristine $BiFeO_3$ ideally suits our purposes as a reference material for the theoretical fitting. The compounds with larger content of La ions are characterized by the orthorhombic phases without remnant polarization at room temperature and thus beyond the scope of the current study.[33–35]

RESULTS

Experimental results

Structural data obtained for the $BiFeO_3$ compounds during the X-ray diffraction (XRD) and neutron powder diffraction (NPD) measurements confirmed their single-phase rhombohedral structure (*R*-phase), which is stable from room temperature up to approximately 810 °C for the pristine compound and ~780 °C for the doped one. The results of the diffraction measurements show a gradual expansion of the unit cell parameters and a volume increase with temperature increase. Chemical substitution of the bismuth ions by small amount of lanthanum ions (5%) only slightly modifies the structural parameters. We did not observe any notable structural anomaly near the magnetic transition temperature, implying a weak correlation between magnetic order and crystal structure in contrast to ref. 35.

Normalized lattice parameters shown in Fig. 1a, b displays tetragonal-like distortion of the reduced unit cell associated with the polar displacements of the cations directed along the *c*-parameter (in rhombohedral lattice with hexagonal settings). Evolution of the structural parameters estimated for the doped compound shows faster elongation of the *a*-parameter as compared to the *c*-parameter, resulting in a decrease in tetragonality. Temperature dependences of the unit cell volume and tetragonality parameter are shown in Fig. 2a, c.

It is known that doping with lanthanum as well as with other RE elements diminishes the covalency of the Bi(La)–O chemical bond[36, 37] and thus reduces the polar displacements of the cations and the tetragonality of the structure. Reduction in the polar displacement of the lightly doped $Bi_{1-x}RE_xFeO_3$ compounds has been confirmed experimentally by neutron diffraction data as well as piezoresponse force microscopy technique.[38, 39] Taking into account the evolution of tetragonality observed for the compounds, one can estimate the transition temperature of the tetragonal structure to the cubic-like structure at about 1100 °C for the pristine $BiFeO_3$ and about 1000 °C for the doped compound.

It should be noted that the tetragonality estimated for both compounds gradually increases with temperature up to about 500 °C and then quite rapidly reduces down to the value below the calculated one for the room temperature structure. The rhombohedral angle calculated for the pseudo-cubic metric shows the opposite trend with a decrease up to $T \sim 500$ °C followed by gradual increase (see Table S1 in the Supplementary Materials). The critical temperature about 500 °C is also noticed by tracing the evolution of the structural parameters discussed below.

The structural data show that the chemical doping with lanthanum leads to an increase of the rhombohedral angle of the lattice, thus pointing to the reduction of the structural distortion,[34, 40] wherein the tetragonality and the unit cell volume gradually decreases (e.g., for 16% of La compound, the unit cell

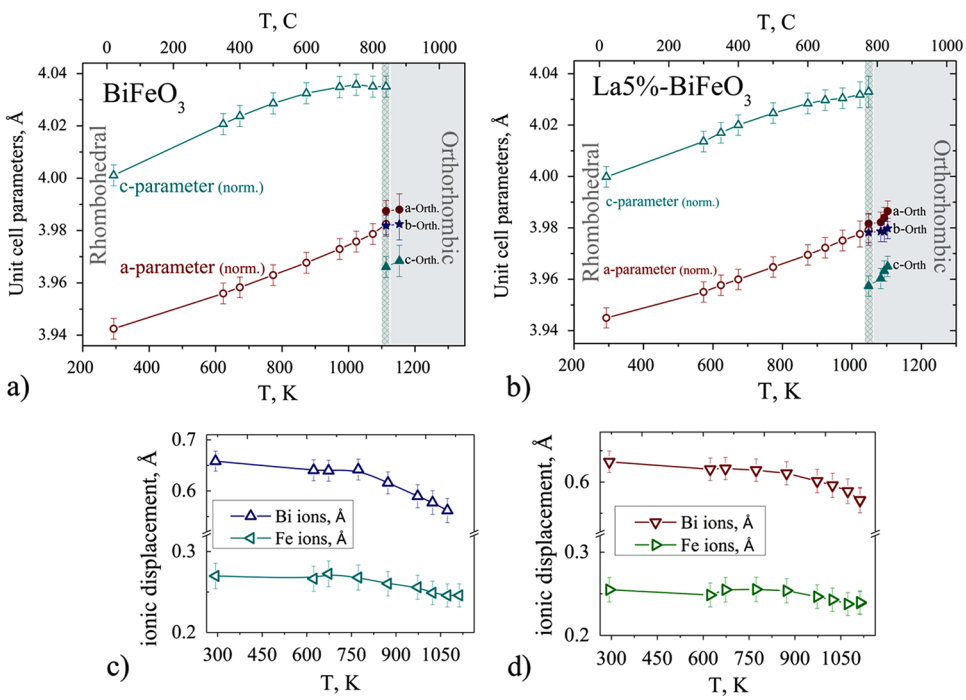

Fig. 1 Temperature evolution of the unit cell parameters and ionic displacements calculated for the pristine (**a**, **c**) and La-doped (**b**, **d**) $BiFeO_3$ compounds based on the NPD data. The rhombohedralorthorhombic transition and temperature region attributed to the orthorhombic phase are highlighted by *gray vertical stripes*

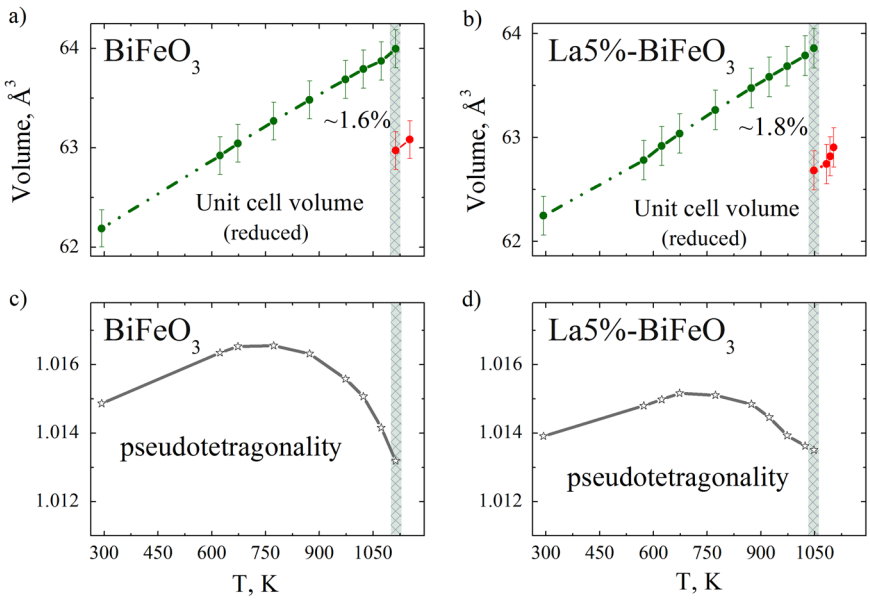

Fig. 2 Temperature evolution of the unit cell volume and tetragonality parameter calculated for the pristine **a**, **c** and La-doped **b**, **d** $BiFeO_3$ compounds based on the NPD data. Gray vertical stripe denotes the rhombohedral-orthorhombic transition)

volume is about 61.7 Å;[3] rhombohedral angle $alfa_{(R)}$ ~ 89.68°). The structural parameters, such as the chemical bond angle Fe–O–Fe, gradually increase with an increase in temperature, while the bond lengths of Fe–O exhibit a different behavior for short and long bonds. The short bond length shows a progressive increase with temperature, while the long bond displays a restoring behavior similar to that observed for the tetragonality parameter and the rhombohedral angle (the inflection point is also about 500 °C). Similar evolution of the structural parameters has been observed for the La-doped compound and the pure compound, thus indicating that the same factors are causing the structural modification observed in both these compounds (Fig. 1b, d). The mentioned structural rearrangement is most probably associated with the oxygen octahedra tilts and rotations, which become more pronounced across the phase transition into the orthorhombic phase as discussed below.

In contrast to the evolution of tetragonality, the magnitude of polar ionic displacement shows a gradual decrease with increase in temperature for both compounds (Figs. 1 and 2). Because of the symmetry restrictions (viz. the presence of the 3-rotation axis in the rhombohedral lattice), the ionic shift is directed strictly along the ***c***-axis of the lattice. The polar displacement calculated for the bismuth ions in the $BiFeO_3$ is about 0.65 Å at room temperature, which leads to a polarization of ~67 μC/cm^2 (assuming simple point charge model); the dipole moment attributed to the doped compound is about 4% smaller, thus resulting in proportionally lower polarization. The difference in the Fe–O bond lengths (the bond lengths for initial compound are 2.115 and 1.943 Å at room temperature) also contributes to the dipole moment of the compounds, accounting about 30% of overall polarization (Fig. S1 in Supplementary Materials). Temperature increase causes a modification of the ionic coordinates (Table S1 in Supplementary Materials) leading to a gradual decrease of the polar displacements of the Bi ions and nearly negligible changes for the Fe ions (Fig. S1 in Supplementary Materials). The reduction in the displacements of the Bi ions becomes more pronounced at high temperatures showing certain anomaly at ~500 °C for the initial compound.

Thermal evolution of the bond lengths Bi(La)–O observed for the pristine bismuth ferrite shows certain anomaly at ~500 °C, followed by faster decrease in the magnitude as compared to the dependence estimated for the doped compound. The difference in the behavior of the ionic displacement is associated with a modification of the character of the chemical bonds because of different covalent component in the Bi(La)–O lengths as confirmed by change density analysis ref. 36. More pronounced covalent component estimated for the initial compound makes it more stable at high temperatures as confirmed by the given structural data. The displacement estimated for the Fe ions shows only slight decrease with temperature increase for both compounds.

Significant displacement of the bismuth/lanthanum ions from their ideal perovskite positions is often associated with anomalous atomic displacement parameters.[41] Refinement of the NPD patterns using anisotropic displacement parameters has considerably improved the reliability factors. The atomic displacement parameters calculated for the rhombohedral phase testify to an elongation of the thermal ellipsoids associated with bismuth/lanthanum ions along the polar axis $[111]_p$.

The NPD patterns recorded for the compounds at high temperatures (~800 °C) have revealed drastic changes in the crystal structure associated with the rhombohedral-orthorhombic phase transition.[42, 43] The diffraction data shows a narrow temperature range (about 20–30 °C) of the two-phase mixture state, thus confirming the high chemical homogeneity of the compounds. Further temperature increase leads to the formation of a single phase state with non-polar orthorhombic symmetry described by the space group *Pnma* (*O*-phase).

The R–O structural transition for the initial compound is observed at ~840 °C; this transition is accompanied by an abrupt decrease in the reduced unit cell parameters, which becomes much closer in their magnitudes resulting in a pseudo-cubic symmetry. The unit cell volume calculated for the pristine compound $BiFeO_3$ shows a drastic decrease (~1.6%); the doped compound also exhibits a comparable decrease in the unit cell volume (~1.8%) (Fig. 1), while the structural transition is shifted towards lower temperature and completes at about 780 °C. The changes of the unit cell parameters across the transition (Fig. 1) as well as the evolution of the polar ionic shifts imply a first-order displacive phase transition into the nonpolar orthorhombic state. Lower transition temperature observed for the doped compound has allowed us to perform reliable refinement of the structural parameters as the diffraction patterns are not deteriorated in quality because of decreased signal-to-noise and chemical decomposition started at T ~ 850 °C for the initial compound.

The diffraction results cannot provide reliable structural data necessary to reveal the origin of these phase transitions, because of uncertainty in the unit cell parameters calculated near the decomposition temperature. To clarify the structural evolution of the compounds at high temperatures, we have performed theoretical modeling of the phase stability of the different crystal structures as well as the estimated presence of the intermediate phases.

Structural data veracity

It is known[44–46] that a substitution of the bismuth ions by lanthanum ones lowers the temperatures of the structural transitions and increases structural stability of the compounds. The DTA/DSC measurements performed in the research have clarified the phase transition temperatures and an application of the obtained results has permitted us to accomplish a careful estimation of the structural parameters based on the neutron diffraction measurements. The phase purity of the compounds has been verified by the diffraction measurements and the obtained structural data are in accordance with the results declared in previous seminal works.[13, 34, 44]

It is known that the chemical decomposition of the pristine compound occurs at about 930 °C[20, 35] while one can assume some release of the oxygen and bismuth ions at lower temperatures; the structural data used for theoretical calculations have been taken at a lower temperature range where any decomposition process is negligible. Moreover, the neutron diffraction process assumes that an interaction of the neutrons with matter occurs in a thick layer of the crystallites (about 100 nm) so that the diffraction data reflect the average structural parameters throughout the grains (not just their surface layers). Taking into account these arguments, one can have high confidence in the reliability of the provided structural results.

Theoretical background

Extraction of the octahedral tilt and polarization. The temperature dependence of the oxygen octahedra tilt has been determined from the full set of oxygen positions, directly extracted from the structural data measured in *R3c* phase in this work. According to refs. 43, 47, for the *R3c* space group, the fractional coordinates of oxygen atoms in the one of 18 equivalent Wyckoff position have the form **O:**$\left(\frac{1}{2}+2e-2d,\quad -4d,\quad 1-s\right)$, where the temperature dependences e, d and s values will be determined from the experiment. Based on the coordinates, we determine the angle of oxygen octahedra tilt as $\omega = \arctan\left(\frac{4\sqrt{3}e}{1-12d}\right)$. In the same coordinate settings, Bi atom has the following fractional coordinates **Bi**: $(0, 0, \frac{1}{4}+s)$. Components of the oxygen atom displacement $\mathbf{\Phi}$ are equal to $\mathbf{\Phi}_1 = \mathbf{\Phi}_2 = \mathbf{\Phi}_3 = \frac{a}{\sqrt{8}}\tan\frac{\omega}{\sqrt{3}} \approx \frac{a}{\sqrt{2}}\frac{2e}{1-12d}$, where a is the lattice constant. Comparison with experiment gives the following values $e \sim -0.03$; $d \sim -0.05$; $s \sim 0.05$ and $\omega \sim 11°$, which vary with temperature as anticipated. The calculated temperature dependence of the oxygen displacement $\mathbf{\Phi}$ for the *R3c* phase is shown in Fig. 3a. Empty and filled diamonds correspond to pure $BiFeO_3$ and $BiFeO_3$ doped with 5% of La respectively.

The temperature dependence of FE polarization was calculated using the following relation $P = \frac{6q_e(q_{Bi}\delta z_{Bi} + q_{Fe}\delta z_{Fe})}{V_{u.c.}}$, where q_e is the elementary charge of electron, $q_{Bi} = 4.38$ and $q_{Fe} = 3.61$ are corresponding Born effective charges taken from,[48] where δz_{Bi} and δz_{Fe} are displacements of Bi and Fe atoms from their centrosymmetric positions, c is the lattice constant along polar axis, and $V_{u.c.}$ is the unit cell volume, $V_{u.c.} = \left(\sqrt{3}/2\right)a^2c$. The factor of "6" takes into account the presence of six formula units inside the unit cell. The temperature dependence of the recalculated spontaneous polarization P in *R3c* phase is shown in Fig. 3b.

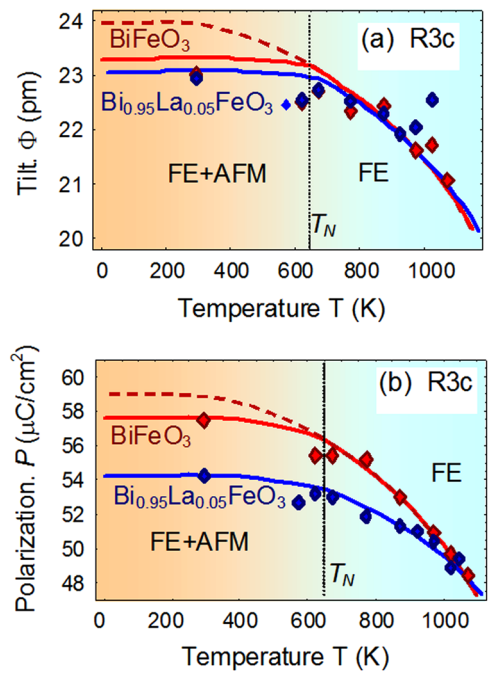

Fig. 3 Temperature dependence of **a** AFD order parameter $\mathbf{\Phi}$ (oxygen displacement from symmetric position) and **b** recalculated spontaneous polarization P in *R3c* phase. *Empty* and *filled diamonds* correspond to experimental results for pure $BiFeO_3$ and doped with 5% of La, respectively measured in this work. *Solid curves* represent the fitting with parameters from the Table 2. *Dashed curves* for BiFeO3 are calculated without biquadratic AFD–AFM and FE–AFM couplings terms

Empty and *filled diamonds* correspond to experimental results for pure $BiFeO_3$ and doped with 5% of La, respectively measured in this work.

Thermodynamic potential. Our primary goal is not only to explain and describe quantitatively the experimental data, but also to construct a thermodynamic potential of LG type, that describes AFM, FE and AFD properties for pure $BiFeO_3$ and $BiFeO_3$ slightly doped with La, including the FE-AFD *R3c* phase, different structural AFD phases (orthorhombic *Pbnm*, tetragonal *I4/mcm*) and cubic *Pm3m* phase. For this purpose, we include the AFD, FE and AFM contributions and the biquadratic coupling among them:

$$\Delta G = \Delta G_{AFD} + \Delta G_{FE} + \Delta G_{AFM} + \Delta G_{BQC} \tag{1}$$

The AFD energy is a six-order expansion on the two tilt vectors ($\mathbf{\Phi}_i$ and $\mathbf{\Psi}_i$):

$$\Delta G_{AFD} = a_i^{(\Phi)}\mathbf{\Phi}_i^2 + a_{ij}^{(\Phi)}\mathbf{\Phi}_i^2\mathbf{\Phi}_j^2 + a_{ijk}^{(\Phi)}\mathbf{\Phi}_i^2\mathbf{\Phi}_j^2\mathbf{\Phi}_k^2 + a_i^{(\Psi)}\mathbf{\Psi}_i^2 + a_{ij}^{(\Psi)}\mathbf{\Psi}_i^2\mathbf{\Psi}_j^2 + a_{ijk}^{(\Psi)}\mathbf{\Psi}_i^2\mathbf{\Psi}_j^2\mathbf{\Psi}_k^2. \tag{2a}$$

Here $\mathbf{\Phi}_i$ and $\mathbf{\Psi}_i$ are components of pseudovectors, determining out-of-phase and in-phase static rotations of oxygen octahedral groups (eigenvectors of AFD modes of lattice vibrations), and Einstein summation convention is employed. These vectors correspond to Glazer tilt systems $a^-b^-c^-$ and $a^+b^+c^+$, respectively and have different transformation properties. AFD order parameters $\mathbf{\Phi}_i$ and $\mathbf{\Psi}_i$ could be measured as either tilt angles of oxygen octahedra or oxygen atoms displacement from the symmetric

Table 1. Experimentally measured transition temperatures of $BiFeO_3$ and $Bi_{0.95}La_{0.05}FeO_3$, collected from the refs. 9, 30, 54 as well as experimental data presented in this work

Mutiferroic	Neel temperature	Transition *R3c-Pbnm*	Transition *Pbnm-I4/mcm*	Transition *I4/mcm-Pm3m*
$BiFeO_3$	645 K	1080–1100 K	1258 K	1356 K
$BiFeO_3$: 5%La	655 K	1040–1080 K	1252 K	1392 K

Table 2. Extracted from the fitting expansion coefficients of the LG potential for $BiFeO_3$ and $Bi_{0.95}La_{0.05}FeO_3$

Parameter	SI units	Value for $BiFeO_3$ (in brackets for *R3c* phase of $Bi_{0.95}La_{0.05}FeO_3$)
$a_T^{(\Phi)}$	J/(m^5 K)	4×10^{26}
T_Φ, $T_{q\Phi}$	K	T_Φ = 1440 (1470 for $Bi_{0.95}La_{0.05}FeO_3$), $T_{q\Phi}$ = 400 (500 for $Bi_{0.95}La_{0.05}FeO_3$)
$a_{ij}^{(\Phi)}$	J/m^7	$a_{11}^{(\Phi)}=-4.53\times10^{49}+4.5\times10^{48}\times\coth(300/T)$, $a_{12}^{(\Phi)}=6.34\times10^{49}-4.5\times10^{48}\times\coth(300/T)$
$a_{ijk}^{(\Phi)}$	J/m^9	$a_{111}^{(\Phi)}=16.72\times10^{70}-3.4\times10^{70}\times\coth(400/T)$, $a_{112}^{(\Phi)}=8.8\times10^{70}-4.0\times10^{67}\times$T, $a_{123}^{(\Phi)}=9.52\times10^{71}-4.32\times10^{71}\times\coth(1200/T)$
$\xi_{ij}^{(\Phi\Psi)}$	J/m^7	$\xi_{11}\geq1.5\times10^{49}$, $\xi_{12}=-1.60\times10^{50}+3.6\times10^{49}\times\coth(300/T)$ (weak coupling in the vicinity of *Pbnm-I4/mcm* transition, strong in *R3c* phase)
$a_T^{(\Psi)}$	J/(m^5 K)	3.2×10^{26}
T_Ψ, $T_{q\Psi}$	K	T_Ψ = 1200, $T_{q\Psi}$ = 200
$a_{ij}^{(\Psi)}$	J/m^7	$a_{11}^{(\Psi)}=3.7\times10^{49}-9\times10^{48}\times T$, $a_{12}^{(\Psi)}>0$
$a_{ijk}^{(\Psi)}$	J/m^9	$a_{111}^{(\Psi)}=12.9\times10^{70}-6\times10^{67}\times$T, $a_{112}^{(\Psi)}>5\times10^{70}$, $a_{123}^{(\Psi)}\geq10^{70}$
$\zeta_{ij}^{(P\Phi)}$	J/(m C^2)	$\zeta_{11}+2\zeta_{12}+\zeta_{44}=-2.1\times10^{29}$, $\zeta_{12}\leq0.7\times10^{29}$, $\zeta_{44}=-3.0\times10^{29}$ (strong coupling)
$\eta_{ij}^{(\Psi P)}$	J/(m C^2)	$\eta_{11}\geq10^{30}$, $\eta_{12}\geq10^{30}$ (very strong coupling)
$a_T^{(P)}$	m J/(K C^2)	0.9×10^6 (0.45×10^6 for $Bi_{0.95}La_{0.05}FeO_3$)
T_C, T_{qP}	K	T_C = 1300 (1360 for $Bi_{0.95}La_{0.05}FeO_3$), T_{qP} = 800
$a_{ij}^{(P)}$	m^{5}J/(C^4)	$a_{11}^{(P)}=-1.35\times10^9$, $a_{12}^{(P)}=0.5\times10^9$
$a_{ijk}^{(P)}$	m^{9}J/(C^6)	$a_{111}^{(P)}=11.2\times10^9$, $a_{112}^{(P)}=-3.0\times10^9$, $a_{123}^{(P)}=-6.0\times10^9$
κ	J/m^5	7.0×10^{28} (9.0×10^{28} for $Bi_{0.95}La_{0.05}FeO_3$) (weak coupling)
λ	J m/C^2	7.1×10^7 (2.9×10^7 for $Bi_{0.95}La_{0.05}FeO_3$) (weak coupling)
a_i^L	SI-magnetic units	$\alpha_{LT}550(\coth(550/T)-\coth(550/645))$, $\alpha_{LT}550(\coth(550/T)-\coth(550/650))$
ε_b	1	15

position in an ideal cubic perovskite structure.

FE energy ΔG_{FE} is a sixth-order expansion on the polarization vector P_i.

$$\Delta G_{FE}=a_i^{(P)}P_i^2+a_{ij}^{(P)}P_i^2P_j^2+a_{ijk}^{(P)}P_i^2P_j^2P_k^2. \quad (2b)$$

Sixth-order expansion on the tilts $\mathbf{\Phi}_i$ (Eq. 2a) is necessary to describe the first-order transition from the cubic *Pm3m* to tetragonal *I4/mcm* phases, and we find that a sixth-order expansions for Ψ_i and P_i are necessary to quantitatively describe the temperature dependence of different order parameters. AFM energy ΔG_{AFM} is a fourth-order expansion in terms of the AFM order parameter vector L_i because this phase transition in $BiFeO_3$ is known to be the second order one.

$$\Delta G_{AFM}=a_i^{(L)}L_i^2+a_{ij}^{(L)}L_i^2L_j^2. \quad (2c)$$

In accordance with the classical LG theory, we assume that the coefficients $a_i^{(\Phi)}$, $a_j^{(\Psi)}$ and $a_k^{(P)}$ are temperature dependent according to Barrett law,[49] $a_i^{(\Phi)}=a_T^{(\Phi)}T_{q\Phi}\left(\coth\left(T_{q\Phi}/T\right)-\left(T_{q\Phi}/T_\Phi\right)\right)$, $a_j^{(\Psi)}=a_T^{(\Psi)}T_{q\Psi}\left(\coth\left(T_{q\Psi}/T\right)-\coth\left(T_{q\Psi}/T_\Psi\right)\right)$ and $a_k^{(P)}=a_T^{(P)}\left(T_{qP}\coth\left(T_{qP}/T\right)-T_C\right)$, where T_Φ, T_Ψ and T_C are corresponding virtual Curie temperatures, $T_{q\Phi}$, $T_{q\Psi}$ and T_{qP} are characteristic temperatures.[50]

As it was shown recently,[51] similar Barrett-type expressions can be used for AFM coefficient $a_i^L(T)$ of pure bismuth ferrite $a_i^L(T)=\alpha_{LT}T_L(\coth(T_L/T)-\coth(T_L/T_N))$ with the Neel temperature T_N = 645 K and characteristic temperature T_L = 550 K. The expression $L\sim\sqrt{a_1^L(T)/a_{11}}$, valid in the isotropic approximation, describes quantitatively both the temperature dependence of the AFM order parameter measured experimentally in $BiFeO_3$ by neutron scattering by Fischer et al.[19] and anomalous AFM contribution to the specific heat behavior near the Neel temperature measured experimentally by Kallaev et al.[52]. The Neel temperature is a bit higher (T_N = 650 K) for $Bi_{0.95}La_{0.05}FeO_3$[53] (see the first column in Table 1, where all observed transition temperatures in $BiFeO_3$ and $Bi_{0.95}La_{0.0}5FeO_3$ are listed).

The AFD–FE–AFM coupling energy ΔG_{BQC} is a biquadratic form of the order parameters L_i, P_i, $\mathbf{\Phi}_i$ and $\mathbf{\Psi}_i$. The detailed forms of these contributions, which account for the parent phase symmetry *Pm3m* of $BiFeO_3$ and different transformation properties of the out-of-phase tilt $\mathbf{\Phi}_i$ and in-phase tilt $\mathbf{\Psi}_i$, are listed in the Appendix B, Supplementary Materials. The short form of ΔG_{BQC} is

$$\Delta G_{BQC}=\xi_{ij}\mathbf{\Phi}_i^2\mathbf{\Psi}_j^2+\zeta_{ijkl}\mathbf{\Phi}_i\mathbf{\Phi}_jP_kP_l+\eta_{ij}\mathbf{\Psi}_i^2P_j^2+\kappa_{ij}\mathbf{\Phi}_i^2L_j^2+\lambda_{ij}P_i^2L_j^2, \quad (2d)$$

For a given symmetry, the coupling energy in Eq. 2d includes nine unknown tensorial coefficients in Voight notation for the AFD–AFD (ξ_{11}, ξ_{12}) and AFD–FE (ζ_{44}, ζ_{11}, ζ_{12}, η_{11} η_{12}) biquadratic

couplings. Due to the lack of experimental data, FE–AFM and AFD–AFM constants λ_{ij} and κ_{ij}[32] are assumed to be isotropic, $\lambda_{ij}=\lambda\delta_{ij}$ and $\kappa_{ij}=\kappa\delta_{ij}$.

Note, that DM interaction was not included in the potential (1), because we have focused on the influence of the simplest and omnipresent biquadratic couplings between the tilt, polarization, and (anti)ferromagnetism. Also we see no serious grounds to include more complex DM-related coupling like $\mathrm{L}\times\mathrm{M}\times\mathrm{P}\times\mathbf{\Phi}$ in the bulk functional, which can be allowed by the symmetry. Also we have neglected all gradient and flexo-type coupling terms, because we restricted ourselves to the consideration of homogeneous bulk $BiFeO_3$.

LG potential coefficients. LG potential coefficients have been determined from experiments using the fitting procedure. The procedure started from the high temperature structural phases (cubic, tetragonal I4/mcm and orthorhombic *Pbnm*) and then goes down to the low temperature FE-rhombohedral *R3c* phase. Expansion coefficients of the LG potential for pure $BiFeO_3$ and $BiFeO_3$ doped with 5% of La extracted from the fitting of measured the AFD and FE order parameters in rhombohedral *R3c*, orthorhombic *Pbnm* and tetragonal *I4/mcm* phases are listed in the Table 2.

Note, that for the complex sequence of the first-order phase transitions, the virtual Curie temperatures T_C, T_Φ and T_Ψ, listed in the Table 2, can be different from the corresponding transition temperatures from *R3c* to *Pbnm* phase, from *Pbnm* to *I4/mcm* phase and from *I4/mcm* to *Pm3m* phase measured experimentally and listed in the Table 1. At the first glance, virtual Curie temperatures, $T_C=(1300–1380)$ K, and $T_\Phi=(1440–1470)$ K listed in the Table 2, seem noticeably higher than the corresponding transition temperatures $T_{FE}=1100$ K and $T_{S2}=(1350–1400)$ K observed experimentally. The temperature $T_\Psi=1200$ K is lower than the transition one, $T_{S1}=1250$ K. Actually, the Curie temperatures should coincide with the transition temperatures only for the single second-order transition between e.g. non-structural cubic paraelectric phase with $P_i=0$ and pure FE phase with $P_j\neq 0$. For the complex sequence of the first-order structural-phase transitions and-polar phase transitions, observed for the $BiFeO_3$ (*R3c* with nonzero $P_1=P_2=P_3\neq 0$ and $\mathbf{\Phi}_1=\mathbf{\Phi}_2=\mathbf{\Phi}_3\neq 0\Rightarrow$ *Pbnm* phase with nonzero $\mathbf{\Phi}_1=\mathbf{\Phi}_2\neq 0$ and $\mathbf{\Psi}_3\neq 0\Rightarrow$ I4/mcm phase with the only nonzero $\mathbf{\Phi}_1\neq 0\Rightarrow$ *Pm3m* phase without any long-range order), the virtual Curie temperatures T_C, T_Φ and T_Ψ can be different from corresponding transition temperatures T_{FE}, T_{S1} and T_{S2} due to the 6th-order nonlinear terms of the order parameter, like $a_{ijk}^{(P)}P_i^2P_j^2P_k^2$ or $a_{ijk}^{(\Phi)}\mathbf{\Phi}_i^2\mathbf{\Phi}_j^2\mathbf{\Phi}_k^2$, as well as due to the transition temperature shifts by the biquadratic (or even bilinear) coupling terms in Eq. 2d.[32, 51] Furthermore, at the transition temperatures from *R3c* and *Pnma*, and from *Pnma* to *I4/mcm*, the two involved phases have the same free energy, and thus usually the transition temperatures are lower than the corresponding Curie temperatures. It appears that the shift caused by the 6th-order nonlinearity is typically small in pure and slightly doped $BiFeO_3$, not more than (10–50) K, but the shift caused by the biquadratic coupling $\zeta_{ijkl}\mathbf{\Phi}_i\mathbf{\Phi}_jP_kP_l$ decreases the virtual Curie temperature T_C by more than 150 K towards experimentally observed value T_{FE}. The difference of about (50–100) K between the observed AFD transition temperatures and corresponding Curie temperatures are mostly related to the coupling between the different structural order parameters described by the term $\xi_{ij}\mathbf{\Phi}_i^2\mathbf{\Psi}_j^2$ in Eq. 2d. Moreover, the coefficients of the nonlinear terms should exhibit temperature dependence in order to have better agreement between the theory and the experiments.

Let us emphasize that an intermediate metastable monoclinic phase with $\mathbf{\Phi}_1=\mathbf{\Phi}_2\neq\mathbf{\Phi}_3$ and $P_1=P_2\neq P_3$ can appear between the rhombohedral and orthorhombic phases (e.g., around (1100–1200 K) in addition to the observed phases. The energy of the monoclinic phase decreases with changing coefficients ζ_{44} and ζ_{12}, (at that ζ_{12} becomes larger with ζ_{44} decrease at the fixed value of $\zeta_{11}+2\zeta_{12}+\zeta_{44}$). The phase may become stable in $BiFeO_3$ slightly doped with Ca or Mn.[54, 55]

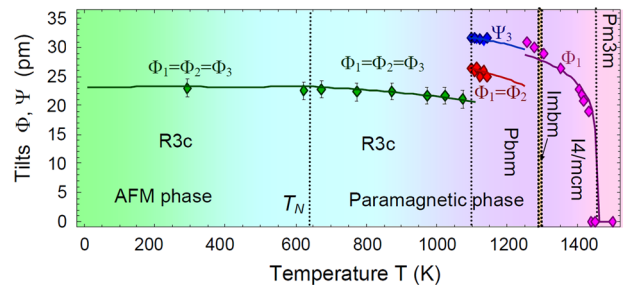

Fig. 4 Temperature dependence of oxygen displacement components for different phases of $BiFeO_3$ along with the fitting (*solid curves*). Symbols of different phases (*R3c*, *Pbnm*, *Imbm*, *I4/mcm*, and *Pm3m*) are specified near the curves. Results for *Pbnm* phase are taken from,[58] tilt for virtual *I4/mcm* phase is from.[59] Fitting parameters are listed in the Table 2

The fitting results, which illustrate how the considered functional fit the experimentally measured temperature dependence of the AFD order parameter and FE polarization in the FE-AFD *R3c* phase of the pure $BiFeO_3$ and $BiFeO_3$ with 5% of La, are shown in the Fig. 3a, b. Note that the temperature dependence of the dielectric permittivity measured by Kamba et al.[56], as well data obtained Lobo et al.[57], was taken into account (Fig. S2c, Supplementary Material), when we chose the optimal fitting parameters for polarization temperature dependence in *R3c* phase. *Dashed curves* for $BiFeO_3$ are calculated without biquadratic AFD–AFM and FE–AFM couplings terms $(\kappa\mathbf{\Phi}^2+\lambda P^2)L^2$. Thus AFD–AFM and FE–AFM couplings are sufficient to cause the small fractures of AFD and FE order parameters at Neel temperature, and to increase their saturation rate in the AFM phase, as shown in Fig. 3a, b. However AFD-AFM and FE-AFM couplings are relatively weak to shift the lowest AFM transition temperature by 645 K towards *R3c-Pbnm* transition at 1100 K. The corresponding temperature dependence of $BiFeO_3$ AFM order parameter (theoretical fitting and the neutron scattering by Fischer et al.[19]) is shown in Fig. S2a, Supplementary Material.

Figure 4 illustrates the temperature dependence of oxygen displacement components ($\mathbf{\Phi}_i$ and $\mathbf{\Psi}_i$) for different phases of $BiFeO_3$. Experimental data of Arnold et al.[58] and ab initio calculation results of Kornev and Bellaiche[59] are compared with our fitting (*solid curves*). Figure 4 shows a pronounced set of the first-order phase transitions. By analyzing the tilt absolute value, we can conclude that the out-of-phase tilt vector $\mathbf{\Phi}$ first appears at the boundary between cubic *Pm3m* and tetragonal *I4/mcm* phases in accordance with the first-order phase transition scenario, and then it mostly rotates at the borders between different structural phases (Fig. S3b, Supplementary Material). Meanwhile another in-phase tilt vector $\mathbf{\Psi}$ exists in the *Pbnm* phase only, and disappears at its boundaries in accordance with the first-order phase transition scenario. The temperature behavior of the out-of-phase and in-phase tilts is similar to that in $CaTiO_3$.

Role of biquadratic couplings. The temperature dependences of the free energies for different phases (tetragonal *I4/mcm*, orthorhombic *Pbnm* and rhombohedral *R3c*, and non-observable "intermediate" *Imbm*) are shown in the Fig. 5a. As one can see from the figure, the predicted "intermediate" *Imbm* phase with $\mathbf{\Phi}_1=\mathbf{\Phi}_2\neq 0$ has the lowest energy in a narrow temperature range between 1305 and 1322 K. However, its energy is almost the same as the energy of the predicted by DFT *I4/mcm* phase. Hence the

phase can be indeed (*meta*) stable in the narrow temperature interval of 17 K width, and we believe that this prediction could be up for debate, similar to the discussion of the intermediate phases separating *R3c* and *Pnma* phases in Ca-doped $BiFeO_3$[46] and pure $CaTiO_3$.[60] Note that this phase (without changing the sequence of other phases) can be eliminated by simultaneously changing the coefficients $a_{12}^{(\Phi)}$ and $a_{112}^{(\Phi)}$ by about 25%, but the changes lead to the visible disagreement between the theoretical curves and measured experimental data, namely in the shift of the phase transition temperature between *R3c* and *Pbnm* phases to 1150 K. In this case, although the *Imbm* phase is thermodynamically stable in the narrow temperature region, it has not been experimentally observed due to the high kinetic energy barriers of the first-order transition from *I4/mcm* to *Imbm* phases.

Hence, we can achieve a quantitative agreement with experimental results for a definite set of values for the expansion coefficients in Eqs. 2a,b,c,d, which satisfy the definite inequalities for the coefficients listed in the Table 2. All the information we extracted about the biquadratic coupling coefficients are listed in the table. Unexpectedly, the temperature dependence of the coupling coefficients ξ_{12} appears noticeable for pure and lightly doped $BiFeO_3$.

The biquadratic coupling strength is estimated in different phases in Appendix B, Supplementary Materials.

The Ψ**Φ**-coupling between in-phase and out-of phase tilts can be regarded strong enough if the following inequality is valid $\left(2a_{11}^{(\Phi)}+a_{12}^{(\Phi)}\right)a_{11}^{(\Psi)} \le \left(\xi_{12}^{(\Phi\Psi)}\right)^2$. The coupling is weak for the opposite sign >> in the inequality. The positive ΨP-coupling is very strong everywhere to prevent the polarization appearance in *Pbnm* phase, because $4\left(a_{11}^{(P)}+a_{12}^{(P)}\right)\left(a_{11}^{(\Psi)}+a_{12}^{(\Psi)}\right) << \left(\eta_{11}^{(\Psi P)}+2\eta_{12}^{(\Psi P)}\right)^2$ under the required condition $\eta_{ij}^{(\Psi P)} \ge 10$.[30] Appeared that the Ψ**Φ**-coupling is weak only in the vicinity of the *Pbnm*-I4 mcm phase transition and becomes relatively noticeable outside it, and strong in *R3c* phase (see *blue area* in Fig. 5b). The coupling between the FE polarization and out-of-phase tilts can be regarded as strong if the following inequality is valid: $4\left(a_{11}^{(P)}+a_{12}^{(P)}\right)\left(a_{11}^{(\Phi)}+a_{12}^{(\Phi)}\right) \le \left(\zeta_{11}^{(\Phi P)}+2\zeta_{12}^{(\Phi P)}+\zeta_{44}^{(\Phi P)}\right)^2$. Conversely, this coupling can be regarded as weak for the opposite sign ">>" of the inequality. It appears that the P**Φ**-coupling is very strong for the entire *R3c* phase (see Fig. 5c).

Note that a trigger-type phase transition is possible only for the sufficiently large negative value of the coupling coefficient.[28] Since the best fitting corresponds to an unexpectedly strong Ψ**Φ** and P**Φ**-biquadratic couplings, and some of the coupling coefficients are negative ($\zeta_{11} < 0$, $\zeta_{44} < 0$ and $\xi_{12} < 0$), this result is a strong indication for the trigger-type[28] phase transition between *R3c* and *Pbnm* phases, where three components of polarization ($P_1 = P_2 = P_3$) and one out-of-phase tilt component (**Φ**$_3$) disappear and in-phase tilt (**Ψ**) appear simultaneously. However, the transition between *Pbnm* and I4/mcm phases, where **Ψ** and **Φ**$_2$ disappear, is successive rather than the trigger-type due to the small coupling value in the temperature range and possible existence of intermediate *Imbm* phase within a super narrow temperature range. The transition from *I4/mcm* to *Pm3m* phase may be of a trigger-type, if the transition were of the second order. However the suggestion contradicts to Kornev et al. results for tetragonal phase.[59]

Substitution of La doping by other dopants. Chemical doping with RE elements leads to the decrease of the phase transitions temperatures and increases the structural stability of these compounds. The obtained results testify close Landau-Ginzburg-Devonshire (LGD) coefficients for both initial and slightly La-doped BFO compounds [see Table 2]. The result allows us to expand our theoretical approach to the case of other dopants. It is assumed that addition of the small amount "*x*" (less than 5%) of RE doping affects the potential expansion coefficients of BFO and LGD in a linear way, $a_i^{(P,\Phi,\Psi)}(x,T)=a_i^{(P,\Phi,\Psi)}(0,T)+x\delta a_i^{(P,\Phi,\Psi)}$, due to the joint action of electrostriction and rotostriction couplings, and Vegard strains (other name is chemical pressure)[20] produced by the dopants and/or vacancies inclusion.[16–18, 61] The Vegard strains δu_{ij} can be written as the product of Vegard tensor coefficients W_{ij} and the instant dopant concentration $x(\mathbf{r})$, $\delta u_{ij}(\mathbf{r}) = W_{ij}x(\mathbf{r})$. Allowing for electrostriction and rotostriction couplings, the coefficients $\delta a_i^{(P,\Phi,\Psi)}$ are proportional to the convolution of the electrostriction (Q_{ijkl}) and rotostriction (R_{ijkl}) tensor coefficients with the Vegard strains, namely that the corresponding terms are $x\delta a_i^{(P)}=Q_{iikl}\delta u_{kl}(\mathbf{r}) \cong Q_{iikl}W_{kl}x(\mathbf{r})$, $x\delta a_i^{(\Phi)}=R_{iikl}^{(\Phi)}\delta u_{kl}(\mathbf{r}) \cong R_{iikl}^{(\Phi)}W_{kl}x(\mathbf{r})$ and $x\delta a_i^{(\Psi)}=R_{iikl}^{(\Psi)}\delta u_{kl}(\mathbf{r}) \cong R_{iikl}^{(\Psi)}W_{kl}x(\mathbf{r})$. Our approach reconstructs the coefficients $a_i^{(P,\Phi,\Psi)}(0,T)$, while the coefficients $\delta a_i^{(P,\Phi,\Psi)}$ can be calculated (for a definite doping) in a straightforward way if the tensors W_{ij}, Q_{ijkl} and R_{ijkl} are known from microscopic calculations or experiments, where not only the amount of RE dopant, but also the degree of non-stoichiometry (e.g., the vacancies concentration) is controlled with high accuracy. The non-stoichiometry control is especially important because it can affect the free energy coefficients via electrostriction and rotostriction coupling with the Vegard strains produced by the vacancies similarly to the doping effect.

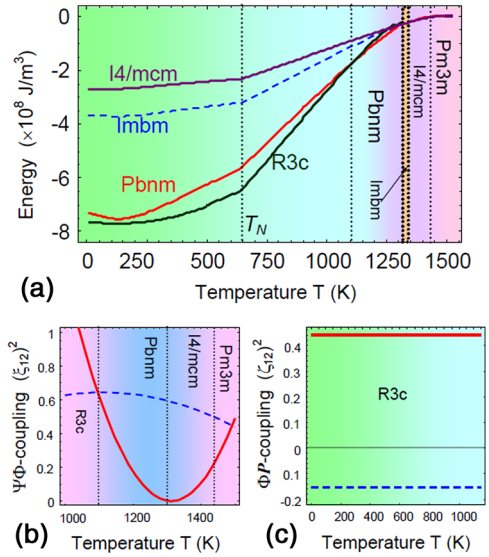

Fig. 5 **a** Temperature dependence of different phases' energies, whose symbols (observable *R3c*, *Pbnm*, *4/mcm*, and non-observable *Imbm*) are specified near the curves. The predicted *Imbm* phase is shown by *filled rectangle* that has about 17 K width. Fitting parameters are listed in Table 2. **b** The *red solid curve* is[26] the biquadratic coupling coefficient squire $\left(\xi_{12}^{(\Phi\psi)}\right)^2$ and the *blue dashed* curve is the temperature dependence of the product $\left(2a_{11}^{(\Phi)}+a_{12}^{(\Phi)}\right)a_{11}^{(\Psi)}$ **c**. The *red solid curve* is the biquadratic coupling coefficients square $\left(\zeta_{11}^{(\Phi P)}+2\zeta_{12}^{(\Phi P)}+\zeta_{44}^{(\Phi P)}\right)^2$ and the *blue dashed curve* is the temperature dependence of the product $4\left(a_{11}^{(P)}+a_{12}^{(P)}\right)\left(a_{11}^{(\Phi)}+a_{12}^{(\Phi)}\right)$

DISCUSSION

To resume the theoretical results, we can state that using the experimental temperature dependences obtained in this work,

together with other independently available experimental data and ab initio calculations, we develop a LG type thermodynamic potential of pristine and slightly doped bismuth ferrite that describes quantitatively their multiferroic phase diagrams with the AFM (below 645 K) and FE-AFD *R3c* (below 1100 K) phases, different structural AFD phases (orthorhombic *Pbnm* at 1100 K < T < 1250 K, tetragonal I4/mcm 1250 K < T < 1350 K) and cubic parent *Pm3m* phase at $T > (1350–1400\ K)$.

By the fitting to experiment and ab initio data for the temperature behavior of the sub-lattice magnetization L, FE polarization P, out-of-phase and in-phase octahedral tilts $\mathbf{\Phi}$ and $\mathbf{\Psi}$, we determined the full set of 4-6-6-LG thermodynamic expansion coefficients, some of which reveal a rather strong temperature dependence. As anticipated, the Barrett-type temperature dependences appear to be valid for all generalized stiffness $\alpha_i(T)$ determining the "isotropic" quadratic terms like $\alpha_L(T)L^2$, $\alpha_P(T)P^2$, $\alpha_\Phi(T)\mathbf{\Phi}^2$ and $\alpha_\Psi(T)\mathbf{\Psi}^2$. Unexpectedly, some of the tensorial expansion coefficients of 4th and 6th order structural terms $a_{ij}^{(\Phi)}\mathbf{\Phi}_i^2\mathbf{\Phi}_j^2$, $a_{ijk}^{(\Phi)}\mathbf{\Phi}_i^2\mathbf{\Phi}_j^2\mathbf{\Phi}_k^2$, $a_{ij}^{(\Psi)}\mathbf{\Psi}_i^2\mathbf{\Psi}_j^2$, and $a_{ijk}^{(\Psi)}\mathbf{\Psi}_i^2\mathbf{\Psi}_j^2\mathbf{\Psi}_k^2$ the coupling coefficients $\xi_{ij}\mathbf{\Phi}_i^2\mathbf{\Psi}_j^2$ should have specific (e.g., linear or saturating) temperature dependences. Therefore, a conventional LG-theory first developed for primary ferroics with the second-order phase transitions, that postulated the temperature-dependent coefficient only for the 2nd order coefficients $\alpha_L(T)$, $\alpha_P(T)$, and $\alpha_\Phi(T)$, is insufficient for multiferroics with the strong interactions between different order parameters.

Hence we conclude that the AFD part of $BiFeO_3$ thermodynamic potential is much more complex than the one in $CaTiO_3$[50] that is a primary ferroic. Moreover, the strong biquadratic AFD-type coupling between the AFD, polar and AFM sub-systems is critical to the quantitative description of the available experimental data for both pristine and slightly doped with La bismuth ferrite. Keeping in mind that the trigger-type phase transitions originate from the same ion contributions, the strong interaction between different order parameters can be expected. Since the best fitting for $BiFeO_3$ corresponds to the unexpectedly strong $\Psi\mathbf{\Phi}$ and $P\mathbf{\Phi}$-biquadratic couplings and some of the coupling coefficients are negative ($\zeta_{11} < 0$, $\zeta_{44} < 0$ and $\xi_{12} < 0$), this result is the independent and rather strong support for a trigger-type[28] phase transition between *R3c* and *Pbnm* phases.

X-Ray and NPD measurements determine a full set of the unit cell parameters, bond angles, and lengths, as well as the ionic displacements in pristine and slightly doped with 5% La bismuth ferrite. The structural parameters, FE polarization and AFD octahedral tilt have been extracted from the measured data in the temperature range 300–1150 K. The experimental data and the results of the theoretical modeling are integrated to determine the evolution of the FE and AFD long-range order parameters, thermodynamic potentials and coefficients across the temperature-driven phase transition into the nonpolar structural phase. The obtained data have detailed the structural phase diagram, focusing on high temperature phases, which could not be observed experimentally because of the decomposition process. In particular, a new structural phase described by space group *Imbm* has been predicted.

Using the experimental results obtained in this work, together with other independent available experimental data and ab initio calculations, we have developed a LG type thermodynamic potential of pristine and slightly doped bismuth ferrite that describes quantitatively their multiferroic phase diagrams with the AFM and FE-AFD *R3c* phases, different structural AFD phases and cubic parent phase. We have proved a trigger-type transition between *R3c* and *Pbnm* phases. We are confident that this transition happens without any "virtual" intermediate phase appearance. The well-pronounced and temperature-separated trigger-type transitions are surprisingly uncommon for ferroic AFD FEs. Complementary to the trigger-type transition, which are surprisingly uncommon for ferroic AFD FEs, we have predicted new intermediate phase described by *Imbm* phase between *Pbnm* and *I4/mcm* phases. The impossibility of avoiding this phase proves that the transition between *Pbnm* and *I4/mcm* cannot be of a trigger-type, as regarded previously.

Based on the obtained experimental data, we have extracted the spontaneous polarization of $BiFeO_3$ in *R3c* phase and estimated AFD parameters including AFD-type biquadratic couplings across the phase transition into the orthorhombic phase for the first time. Furthermore, we have proved that "rotomagnetic" AFD-AFM coupling is very important to describe the FE polarization and AFD tilt behavior in the *R3c* phase of $BiFeO_3$. The coupling was neither considered for $BiFeO_3$, nor probed experimentally for other perovskites, while it was predicted for $EuTiO_3$.[32]

The benefit of the LG-type thermodynamic potential is not only in its capability to describe the observed sequence of the phase transitions along with the temperature behavior of the order parameters, corresponding susceptibilities to external stimuli in the one of the most promising multiferroic, but also it opens the way to model theoretically polar and antiferrodistoritive properties in thin films and nanoparticles of pristine and slightly doped with RE ions bismuth ferrite by incorporating the effect of the interfacial energy and electrostrictive interaction.[12]

METHODS

Ceramic samples of La-doped $BiFeO_3$ with dopant concentrations $x = 0$, 0.05 were prepared by the two-stage solid-state reaction using high purity oxides (Alfa Aesar) as described in refs 40, 62. The oxides Bi_2O_3, La_2O_3, and Fe_2O_3 taken in stoichiometric ratio were thoroughly mixed using a planetary ball mill (Retsch PM 200). Pure $BiFeO_3$ was synthesized at 870 °C for 10 min. La-Doped compound was prepared at 950 °C for 15 h. The XRD patterns were collected at room temperature using a Rigaku D/MAX-B diffractometer (Cu-K_α radiation) equipped with an Anton Paar heating stage. NPD measurements were performed with the high-resolution neutron powder diffractometer FIREPOD ($\lambda = 1.7982$ Å, E9 instrument, HZB). Diffraction data were analyzed by the Rietveld method using the FullProf software package.[63] Thermal analysis was carried out using differential scanning calorimeter Mettler Toledo 822e in argon atmosphere.

ACKNOWLEDGEMENTS

The work of D.V.K., M.V.S., S.A.G. and I.O.T. was supported by the Russian Science Foundation (project # 15-19-20038). Neutron diffraction experiments have been supported by the European Commission under the 7th Framework Programme through the 'Research Infrastructure' action of the 'Capacities' Programme, NMI3-II Grant number 283883'. The work at Penn State is supported by the U.S. Department of Energy, Office of Basic Energy Sciences, Division of Materials Sciences and Engineering under Award FG02-07ER46417 (FX and LQC) and by the NSF MRSEC under Grant No. DMR-1420620 (F.X. and V.G.). A.N.M. and E.A.E. acknowledge the Center for Nanophase Materials Sciences, which is a DOE Office of Science User Facility, CNMS2016-061.

AUTHOR CONTRIBUTIONS

D.V.K., I.O.T., A.F. and M.V.S. conducted structural measurements and wrote the experimental part of the paper. E.A.E. and F.X. performed theoretical calculations, supervised by M.D.G., V.G. and L.Q.C., I.O.T. and S.A.G. prepared the samples. A.N.M. proposed theoretical research ideas and formulated the problem, wrote the introductive, theoretical and discussion parts of the paper. All co-authors densely worked on the results analyses and text improvements.

COMPETING INTERESTS

The authors declare no competing financial interests.

REFERENCES

1. Fiebig, M. Revival of the magnetoelectric effect. *J. Phys. D Appl. Phys* **38**, R123–R152 (2005).
2. Spaldin, N. A. & Fiebig, M. The renaissance of magnetoelectric multiferroics. *Science* **309**, 391–392 (2005).
3. Rondinelli, J. M. & Spaldin, N. A. Structure and properties of functional oxide thin films: insights from electronic structure calculations. *Adv. Mater.* **23**, 3363–3381 (2011).
4. Pyatakov, A. P. & Zvezdin, A. K. Magnetoelectric and multiferroic media. *Phys. Usp.* **55**, 557–581 (2012).
5. Scott, J. F. Data storage: multiferroic memories. *Nat. Mater.* **6**, 256–257 (2007).
6. Seidel, J. et al. Domain wall conductivity in La-doped $BiFeO_3$. *Phys. Rev. Lett.* **105**, 197603–197605 (2010).
7. He, Q. et al. Magnetotransport at domain walls in $BiFeO_3$. *Phys. Rev. Lett.* **108**, 067203–067206 (2012).
8. Catalan, G., Seidel, J., Ramesh, R. & Scott, J. F. Domain wall nanoelectronics. *Rev. Mod. Phys.* **84**, 119–156 (2012).
9. Wang, J. B. N. J. et al. Epitaxial $BiFeO_3$ multiferroic thin film heterostructures. *Science* **299**, 1719–1722 (2003).
10. Maksymovych, P. et al. Ultrathin limit and dead-layer effects in local polarization switching of $BiFeO_3$. *Phys. Rev. B Condens. Matter* **85**, 014119–014116 (2012).
11. Beekman, C. et al. Ferroelectric self -poling, switching, and monoclinic domain configuration in $BiFeO_3$ thin films. *Adv. Funct. Mater.* **26**, 5166–517 (2016).
12. Xue, F., Li, Y., Gu, Y., Zhang, J. & Chen, L.-Q. Strain phase separation: formation of ferroelastic domain structures. *Phys. Rev. B Condens. Matter* **94**, 220101(R) (2016).
13. Kan, D. et al. Universal behavior and electric-field-induced structural transition in rare-earth-substituted $BiFeO_3$. *Adv. Funct. Mater.* **20**, 1108–1115 (2010).
14. Minh, N. V. & Quan, N. G. Structural, optical and electromagnetic properties of $Bi_{1-x}Ho_xFeO_3$ multiferroic materials. *J. Alloys Compd.* **509**, 2663–2666 (2011).
15. Borisevich, A. Y. et al. Atomic-scale evolution of modulated phases at the ferroelectric–antiferroelectric morphotropic phase boundary controlled by flexoelectric interaction. *Nat. Commun.* **3**, 775 (2012).
16. Sankara, P. S. et al. Misfit strain driven cation inter-diffusion across an epitaxial multiferroic thin film interface. *J. Appl. Phys.* **115**, 054103 (2014).
17. Maran, R. et al. Interface control of a morphotropic phase boundary in epitaxial samarium-modified bismuth ferrite superlattices. *Phys. Rev. B Condens. Matter* **90**, 245131 (2014).
18. Maran, R. et al. Enhancement of dielectric properties in epitaxial bismuth ferrite–bismuth samarium ferrite superlattices. *Adv. Electron. Mater.* **2**, 1600170 (2016).
19. Fischer, P., Polomska, M., Sosnowska, I. & Szymanski, M. Temperature dependence of the crystal and magnetic structures of $BiFeO_3$. *J. Phys. C Solid State Phys.* **13**, 1931–1940 (1980).
20. Catalan, G. & Scott, J. F. Physics and applications of bismuth ferrite. *Adv. Mater.* **21**, 2463–2485 (2009).
21. Smolenskiĭ, G. A. & Chupis, I. E. Ferroelectromagnets. *Sov. Phys. Usp.* **25**, 475 (1982).
22. Balke, N. et al. Enhanced electric conductivity at ferroelectric vortex cores in $BiFeO_3$. *Nat. Phys* **8**, 81–88 (2012).
23. Morozovska, A. N., Vasudevan, R. K., Maksymovych, P., Kalinin, S. V. & Eliseev, E. A. Anisotropic conductivity of uncharged domain walls in $BiFeO_3$. *Phys. Rev. B Condens. Matter* **86**, 085315–085313 (2012).
24. Kim, Y. M. et al. Interplay of octahedral tilts and polar order in $BiFeO_3$ films. *Adv. Mater.* **25**, 2497–2504 (2013).
25. Vasudevan, R. K. et al. Domain wall conduction and polarization-mediated transport in ferroelectrics. *Adv. Funct. Mater.* **23**, 2592–2616 (2013).
26. Kim, Y. M. et al. Direct observation of ferroelectric field effect and vacancy-controlled screening at the $BiFeO_3$/LaxSr$_{1-x}MnO_3$ interface. *Nat. Mater.* **13**, 1019–1025 (2014).
27. Winchester, B. et al. Electroelastic fields in artificially created vortex cores in epitaxial $BiFeO_3$ thin films. *Appl. Phys. Lett.* **107**, 052903 (2015).
28. Holakovský, J. A new type of the ferroelectric phase transition. *Phys. Status Solidi B* **56**, 615–619 (1973).
29. Scott, J. F. Iso-structural phase transitions in $BiFeO_3$. *Adv. Mater.* **22**, 2106–2107 (2010).
30. Gopalan, V. & Litvin, D. B. Rotation-reversal symmetries in crystals and handed structures. *Nat. Mater.* **10**, 376–381 (2011).
31. Uwe, H. & Sakudo, T. Stress-induced ferroelectricity and soft phonon modes in SrTiO3. *Phys. Rev. B Condens. Matter* **13**, 271–286 (1976).
32. Eliseev, E. A., Glinchuk, M. D., Gopalan, V. & Morozovska, A. N. Rotomagnetic couplings influence on the magnetic properties of antiferrodistortive antiferromagnets. *J. Appl. Phys.* **118**, 144101 (2015).
33. Suresh, P. & Srinath, S. Effect of La substitution on structure and magnetic properties of sol-gel prepared $BiFeO_3$. *J. Appl. Phys.* **113**, 17D920 (2013).
34. Rusakov, D. A. et al. Structural evolution of the $BiFeO_3$–$LaFeO_3$ system. *Chem. Mater.* **23**, 285–292 (2010).
35. Selbach, S. M., Tybell, T., Einarsrud, M. A. & Grande, T. The ferroic phase transitions of $BiFeO_3$. *Adv. Mater.* **20**, 3692–3696 (2008).
36. Fujii, K. et al. Experimental visualization of the Bi–O covalency in ferroelectric bismuth ferrite $BiFeO_3$ by synchrotron X-ray powder diffraction analysis. *Phys. Chem. Chem. Phys.* **15**, 6779–6782 (2013).
37. Karpinsky, D. V. et al. Evolution of electromechanical properties of $Bi_{1-x}Pr_xFeO_3$ solid solutions across the rhombohedral–orthorhombic phase boundary: Role of covalency. *J. Alloys Compd.* **638**, 429–434 (2015).
38. Levin, I. et al. Displacive phase transitions and magnetic structures in Nd-substituted $BiFeO_3$. *Chem. Mater.* **23**, 2166–2175 (2011).
39. Karpinsky, D. V. et al. Temperature and composition-induced structural transitions in $Bi_{1-x}La(Pr)_xFeO_3$ ceramics. *J. Am. Ceram. Soc.* **97**, 2631–2638 (2014).
40. Karpinsky, D. V. et al. Evolution of crystal structure and ferroic properties of La-doped $BiFeO_3$ ceramics near the rhombohedral-orthorhombic phase boundary. *J. Alloys Compd.* **555**, 101–107 (2013).
41. Shoemaker, D. P., Seshadri, R., Tachibana, M. & Hector, A. L. Incoherent Bi off-centering in $Bi_2Ti_2O_6O'$ and $Bi_2Ru_2O_6O'$: Insulator versus metal. *Phys. Rev. B Condens. Matter* **84**, 064117 (2011).
42. Arnold, D. C., Knight, K. S., Catalan, G., Redfern, S. A. & Scott, J. F. The β-to-γ Transition in $BiFeO_3$: A powder neutron diffraction study. *Adv. Funct. Mater.* **20**, 2116–2123 (2010).
43. Palewicz, A., Przeniosło, R., Sosnowska, I. & Hewat, A. W. Atomic displacements in $BiFeO_3$ as a function of temperature: neutron diffraction study. *Acta Crystallogr. B Struct. Sci.* **63**, 537–544 (2007).
44. Karimi, S., Reaney, I. M., Han, Y., Pokorny, J. & Sterianou, I. Crystal chemistry and domain structure of rare-earth doped $BiFeO_3$ ceramics. *J. Mater. Sci.* **44**, 5102 (2009).
45. Arnold, D. C. Composition-driven structural phase transitions in rare-earth-doped $BiFeO_3$ ceramics: a review". *IEEE Trans. Ultrason. Ferroelectr. Freq. Control* **62**, 62–82 (2015).
46. Khomchenko, V. A., Troyanchuk, I. O., Többens, D. M., Sikolenko, V. & Paixão, J. A. Composition-and temperature-driven structural transitions in $Bi_{1-x}Ca_xFeO_3$ multiferroics: a neutron diffraction study. *J. Phys. Condens. Matter* **25**, 135902 (2013).
47. Megaw, H. D. & Darlington, C. N. W. Geometrical and structural relations in the rhombohedral perovskites. *Acta Crystallogr. A* **31**, 161–173 (1975).
48. Okuno, Y. & Sakashita, Y. Born effective charges and piezoelectric coefficients of $BiXO_3$. *Jpn. J. Appl. Phys.* **48**, 09KF04 (2009).
49. Barrett, J. H. Dielectric constant in perovskite type crystals. *Phys. Rev.* **86**, 118–120 (1952).
50. Gu, Y., Rabe, K., Bousquet, E., Gopalan, V. & Chen, L. Q. Phenomenological thermodynamic potential for $CaTiO_3$ single crystals. *Phys. Rev. B Condens. Matter* **85**, 064117 (2012).
51. Morozovska, A. N., Khist, V. V., Glinchuk, M. D., Gopalan, V. & Eliseev, E. A. Linear antiferrodistortive-antiferromagnetic effect in multiferroics: physical manifestations. *Phys. Rev. B Condens. Matter* **92**, 054421 (2015).
52. Kallaev, S. N. et al. Heat capacity and dielectric properties of multiferroics $Bi_{1-x}Gd_xFeO_3$ (x=0–0.20). *Phys. Solid State* **56**, 1412–1415 (2014).
53. Amirov, A. A. et al. Specific features of the thermal, magnetic, and dielectric properties of multiferroics $BiFeO_3$ and $Bi_{0.95}La_{0.05}FeO_3$. *Phys. Solid State* **51**, 1189–1192 (2009).
54. Karpinsky, D. V. et al. Structural and magnetic phase transitions in $Bi_{1-x}Ca_xFe_{1-x}Mn_xO_3$ multiferroics. *J. Alloys Compd.* **692**, 955–960 (2017).
55. Karpinsky, D. V. et al. Crystal structure and magnetic properties of $Bi_{1-x}Ca_xFe_{1-x}Mn(Ti)_xO_3$ ceramics across the phase boundary. *J. Mater. Sci.* **51**, 10506–10514 (2016).
56. Kamba, S. et al. Infrared and terahertz studies of polar phonons and magneto-dielectric effect in multiferroic $BiFeO_3$ ceramics. *Phys. Rev. B Condens. Matter* **75**, 024403 (2007).
57. Lobo, R. P. S. M., Moreira, R. L., Lebeugle, D. & Colson, D. Infrared phonon dynamics of a multiferroic $BiFeO_3$ single crystal. *Phys. Rev. B Condens. Matter* **76**, 172105 (2007).
58. Arnold, D. C., Knight, K. S., Morrison, F. D. & Lightfoot, P. Ferroelectric-paraelectric transition in $BiFeO_3$: crystal structure of the orthorhombic β phase. *Phys. Rev. Lett.* **102**, 027602 (2009).
59. Kornev, I. A. & Bellaiche, L. Nature of the ferroelectric phase transition in multiferroic $BiFeO_3$ from first principles. *Phys. Rev. B Condens. Matter* **79**, 100105 (2009).
60. Kennedy, B. J., Howard, C. J. & Chakoumakos, B. C. Phase transitions in perovskite at elevated temperatures - a powder neutron diffraction study. *J. Phys. Condens. Matter* **11**, 1479 (1999).
61. Morozovska, A. N. et al. Defect thermodynamics and kinetics in thin strained ferroelectric films: the interplay of possible mechanisms. *Phys. Rev. B Condens. Matter* **89**, 054102 (2014).

62. Troyanchuk, I. O. et al. Phase transitions, magnetic and piezoelectric properties of rare-earth-substituted $BiFeO_3$ ceramics. *J. Am. Ceram. Soc.* **94**, 4502–4506 (2011).
63. Rodríguez-Carvajal, J. Recent advances in magnetic structure determination by neutron powder diffraction. *Phys. B* **192**, 55–69 (1993).

Supplementary Information accompanies the paper on the *npj Computational Materials* website (doi:10.1038/s41524-017-0021-3).